Journal of Materials Chemistry

Cite this: J. Mater. Chem., 2012, 22, 17878

www.rsc.org/materials

PAPER

Inkjet-printed gas sensors: metal decorated WO_3 nanoparticles and their gas sensing properties†

Jarmo Kukkola,[a] Melinda Mohl,[a] Anne-Riikka Leino,[a] Géza Tóth,[a] Ming-Chung Wu,[bc] Andrey Shchukarev,[d] Alexey Popov,[e] Jyri-Pekka Mikkola,[df] Janne Lauri,[e] Markus Riihimäki,[g] Jyrki Lappalainen,[a] Heli Jantunen[a] and Krisztián Kordás*[ad]

Received 20th April 2012, Accepted 9th July 2012
DOI: 10.1039/c2jm32499g

Inkjet deposition is an attractive technology to localize nanomaterials in an area-selective manner on virtually any kind of surfaces. Great advantages of the method are effective usage of materials, low processing temperatures and few required manufacturing steps, thus enabling rapid prototyping and bulk production with reasonably low cost. A number of different electrical devices such as light emitting diodes, transistors and solar cells have already been demonstrated, reflecting the versatility of inkjet printing. In this paper, we collect the contemporary results on inkjet deposited gas sensors and show examples of such gas sensing devices based on surface modified WO_3 nanoparticles for efficient discrimination of various gaseous analytes from sub-ppm up to nearly 0.1% concentration levels in air.

1. Introduction

Gas sensors based on semiconducting metal oxides are indispensable devices that can be applied in diverse segments of our daily life, including automotive exhausts, the household, healthcare as well as industrial processes and safety control systems. The active gas sensing components are usually integrated by using scalable methods such as thick film (gravure- and screen-printing) techniques or CMOS (complementary metal-oxide-semiconductor) compatible techniques (sputtering, evaporation). However, inkjet printing, being one of the most facile deposition tools, is quite untouched in the open literature from the viewpoint of building gas sensors with inorganic semiconducting nanoparticles,[1,2] while several other types of inkjet printed gas sensors are discussed in detail (Table 1).

Various forms of tungsten oxide materials (micro/nanoparticles, wires/rods, thin and porous films) have been synthesized and studied as gas sensing materials during the past few decades, mostly due to their sensitivity towards nitric oxides.[3–5] Pulsed laser deposition,[6] reactive evaporation,[7] sputtering,[8] thermal oxidation,[9] and wet chemical processes[10] are most commonly applied to construct the sensing layers. Decoration and/or doping of semiconducting metal oxides with metal nanoparticles have been known to alter the electrical transport behaviour as well as sensitivity of gas sensors towards different analytes.[11–15] Doping results in the appearance of new impurity levels near the valence and/or conduction bands which can influence both inter- and intra-band carrier transport[16–18] and also alter carrier concentration and mobility. As a result of this, the Debye length of the material is affected. On the other hand, decoration of the semiconductor surface with metals or other semiconducting particles may lead to the formation of rectifying Schottky junctions at the interfaces (depending on the electron affinity of semiconductors and work functions of metals) helping charge separation nearby the anchored nanoparticles also influencing the gas–solid interaction and sensing (electronic sensitization). In addition, the decorating nanoparticles can also activate gas molecules to react with the semiconducting oxide support thus changing the work function and the overall carrier distribution of the surface (chemical sensitization or chemisorption). The classical example of this kind of behaviour is exemplified by the dissociation of H_2 on Pt or on Pd surfaces, followed by a spill over of hydrogen on the support where it partially reduces the oxide surface.[19]

In this work, we study inkjet deposited Taguchi-type gas sensor devices based on various types of surface modified WO_3 nanoparticles. Efficient discrimination of gaseous analytes in air is demonstrated showing the feasibility of developed nanomaterials and also the practical use of inkjet printing in this context.

[a]Microelectronics and Materials Physics Laboratories, Department of Electrical Engineering, University of Oulu, Oulu FI-90570, Finland. E-mail: lapy@ee.oulu.fi; Fax: +358 (8) 5532 728; Tel: +358 (8) 5532 723
[b]Department of Materials Science and Engineering, National Taiwan University, Taipei 106-17, Taiwan, China
[c]Department of Chemical and Materials Engineering, Chang Gung University, Tao-Yuan 333-02, Taiwan, China
[d]Technical Chemistry, Department of Chemistry, Umeå University, Umeå SE-90187, Sweden
[e]Optoelectronics and Measurement Techniques Laboratory, Department of Electrical Engineering, University of Oulu, Oulu FI-90570, Finland
[f]Industrial Chemistry and Reaction Engineering, Process Chemistry Centre, Åbo Akademi University, Turku FI-20500, Finland
[g]Mass and Heat Transfer Process Laboratory, Department of Process and Environmental Engineering, University of Oulu, Oulu FI-90570, Finland
† Electronic supplementary information (ESI) available. See DOI: 10.1039/c2jm32499g

Table 1 Comparison of different types of inkjet printed gas sensors[a]

Active material	Sensing principle	Analyte (sensitivity)	Lowest conc. measured	Ref.
Polystyrene/carbon black	Resistive	CH_3COCH_3 ($\Delta R/R$, $\sim 2 \times 10^{-4}$% per ppm)	600 ppm	20
PABS-SWCNT	RF antenna resonance shift	NH_3 (Δfres, 43 MHz @ 50 ppm)	50 ppm	21
PANI, $CuCl_2$ doped PANI	Resistive	H_2S ($\Delta R/R$, ~ -16% per ppm)	2.5 ppm	22
Reduced graphene oxide	Resistive	NO_2 ($\Delta R/R$, ~ -0.6% per ppm)	0.5 ppm	23
		Cl_2 ($\Delta R/R$, ~ -0.13% per ppm)	6 ppm	
		NH_3, CH_3OH, C_2H_5OH and CH_2Cl_2 ($\Delta R/R$, $\sim$22%, $\sim$10%, $\sim$9% and $\sim$6%, respectively)	Sat. vapors	
SWCNTs	Resistive	CH_3OH ($\Delta R/R$, $\sim$0.02% per ppm)	300 ppm	24
SWCNTs	Resistive	NO_2 ($\Delta R/R$, $\sim$10% per ppm)	50 ppb	25
SWCNTs	Resistive wireless RF-identification tag	NH_3 ($\Delta R/R$, $\sim 2.5 \times 10^{-3}$% per ppm) NH_3 (increased power reflection from -18.4 dB to -7.6 dB at antenna port due to changed impedance in 4% NH_3)	4%	26
PANI	Resistive	NH_3 ($\Delta R/R$, $\sim$0.32% per ppm)	2.5 ppm	27
		H_2S (carbon electrodes, $\Delta R/R$, -0.2% per ppm)	100 ppm	
		H_2S (Ag electrodes, $\Delta R/R$, 2.57% per ppm)	100 ppm	
		NO_x ($\Delta R/R$, -0.2% per ppm)	100 ppm	
		TMA and TEA ($\Delta R/R$, 0.33 and 0.2% per ppm, respectively)	100 ppm	
CNTs	Noise of sensor resistance	N_2O, H_2S, CO, H_2O	50 ppm	28
SWCNTs	Resistive chem-FET	H_2S ($\Delta R/R$, ~ -0.08% per ppm)	100 ppm	29
		H_2S ($\Delta R/R$, ~ -0.37% per ppm)	100 ppm	
UV-curable polymers	Resistive	H_2O vapor (exponential decrease of R with relative humidity)		30
PMAS-SWCNTs	Resistive	CH_3OH, C_2H_5OH, 2-C_3H_7OH, C_4H_9OH, $CHCl_3$ and $C_6H_5CH_3$ ($\Delta R/R$, 56.5%, 31.3%, 10.9%, 6.7%, 0% and 0%, respectively)	3%	31
MWCNTs	Resistive	CH_3OH, C_2H_5OH, 2-C_3H_7OH, NH_3, H_2O ($\Delta R/R$, $\sim$50%, <10%, <10%, $\sim$150% and $\sim$100%)	Sat. vapors	32
Thiophene based polymers	Resistive	CH_3COCH_3, CH_2Cl_2, $C_6H_5CH_3$, and c-C_6H_{12} ($\Delta R/R$ depends on the type of the polymer, typically in the range between 10^{-3}% per ppm)	170 ppm, 30 ppm, 10 ppm and 10 ppm, respectively.	33
PEDOT:PSS	Resistive	CH_3OH and C_2H_5OH ($\Delta R/R$, $\sim -7 \times 10^{-4}$ and $\sim -3 \times 10^{-4}$% per ppm) H_2O vapor (linear with rel. humidity)	2850 ppm	34
Polypyrrole	Resistive	CH_3OH, C_2H_5OH, C_3H_7OH, $CHCl_3$ and C_6H_6 ($\Delta R/R$, 0.018% per ppm, 0.014% per ppm, 0.011% per ppm, 0.008% per ppm and 0.006% per ppm, respectively)	5000 ppm	35
Polymers	Nanomechanical cantilever deflection and principal component analysis	H_2O and C_2H_5OH		36

[a] PABS: polyaminobenzene sulfonic acid, SWCNT: single-walled carbon nanotube, PANI: polyaniline, CNT: carbon nanotube, PMAS: poly(2-methoxyaniline-5-sulfonic acid), MWCNT: multi-walled carbon nanotube, PEDOT: poly(3,4-ethylene dioxythiophene), PSS: polystyrene sulfonated acid, TMA: trimethylamine, and TEA: triethylamine.

2. Experimental

Wet impregnation was used to anchor solid metal precursors on WO_3 nanoparticles (Sigma-Aldrich, <100 nm). To obtain products with 1 wt% nominal metal loading in the process, 15.9 mg $AgNO_3$ (Aldrich, 99.9999%), 28.7 mg $Pd(C_5H_7O_2)_2$ (palladium acetylacetonate, Aldrich, 99%) and 20.2 mg $Pt(C_5H_7O_2)_2$ (platinum acetylacetonate, Aldrich, 99.99%) were dissolved in acetone–water mixture (200 mL, 50/50 vol.%) and mixed with 1.00 g of WO_3 powder applying ultrasonic agitation for 3 hours, followed by stirring for 6 hours, respectively. After evaporating the solvents under N_2 atmosphere (on a hotplate set to ~80 °C), the samples were annealed in air at 300 °C for 2 hours.

Elemental composition of the decorated nanoparticles was assessed by energy-dispersive X-ray spectroscopy (EDX, Inca, Oxford Instruments, installed on a Jeol JSM-6400 scanning electron microscope) measuring at least at 5 different sample locations. X-ray photoelectron spectroscopy (XPS, Kratos Axis Ultra, mono Al Kα X-ray source, analysis area of 0.3×0.7 mm^2, applying charge neutralizer) was used to study the chemical composition as well as the oxidation states of metals anchored on the WO_3 nanoparticles. X-ray diffraction (XRD, Philips PW1380, Cu Kα radiation), energy filtered transmission electron microscopy (EFTEM, Leo 912 Omega, 120 kV), high-resolution transmission electron microscopy (HRTEM, JEOL 2000FX, 200 kV) and field emission scanning electron microscopy (FESEM, Zeiss ULTRA plus) were applied to study the structure of the materials as well as the surface structure/morphology of sensor devices.

The inks were prepared by mixing 100 mL of deionized water with ~230 mg of WO_3 nanoparticles followed by ultrasonic agitation for 3 hours. After 16 hours of natural sedimentation, the supernatant fraction from the top of the container was collected and used for inkjet printing. During ink preparation, neither surfactants nor other additives were used to simplify interpretation of gas sensing results. The concentrations of the collected WO_3 inks were measured to reside in the range of 0.9 ± 0.4 g L^{-1} (Ag–WO_3), 1.5 ± 0.1 g L^{-1} (Pd–WO_3), 1.3 ± 0.2 g L^{-1} (Pt–WO_3), and 1.4 ± 0.1 g L^{-1} (pristine WO_3). The viscosity of the pristine WO_3 ink (measured by a capillary type viscometer with a differential pressure sensor for measuring a pressure drop along the capillary) was similar to that of water, 0.8 ± 0.1 cP at ~25 °C. The particle size distribution and zeta potential of pristine WO_3 nanoparticle ink were measured by a Delsa Nano C particle analyzer (Beckman Coulter, CA, USA). The particle size distribution and ink stability were also studied by an in-lab-made spectroscopic measurement setup.

Microscopic line patterns of the nanomaterials were deposited using an inkjet printer (Dimatix, DMP-2800, ink and substrate temperatures of 30 and 35 °C, respectively, and piezo firing voltage of 9 V). In order to study the properties of the prepared inks, test patterns were deposited on Si substrates 1, 3, 9, and 27 repeated layers with 25 μm drop spacing using 3 different patterns: a droplet in a single location, four droplets in a row with ~0.2 ms and ~1.8 s drying time between jetting of neighbouring droplets. In each case, the layers are allowed to dry at least for 5 seconds, before depositing the next layer. Sensor devices were inkjet printed on Si/SiO_2 substrates having lithographically defined Ti/Pt electrodes. Line patterns of the sensor materials were deposited across the chip electrodes by ejecting 10 ink droplets (10 pL nominal volume) with 20 μm centre-to-centre spacing (while keeping ~1.8 s drying times) between each droplet and then repeating the process to have 20 layers.

After the actual printing, each sensor was exposed to a heating cycle as follows: 300 K–500 K–350 K–500 K–300 K with 10° min^{-1} heating/cooling rates to dry the printouts. Gas response to H_2, NO, CO, and H_2S analytes (in this order) was measured at 220 °C in air buffer using a Labview controlled gas blender. The sensors were heated at a rate of 10° min^{-1} from room temperature up to the operation temperature just before starting the measurement. At the beginning of each gas measurement, the sample was kept at 220 °C for 8 hours under synthetic air atmosphere to clean the surface of the sensors and stabilize the conductance signal. Several gas input cycles, with four different analyte concentrations, were used in the course of the gas measurements. Current–voltage, resistance–temperature and gas sensing experiments were performed in darkness in a Linkam THMS600 Heating and Freezing Stage using a Keithley 2636A sourcemeter and an Agilent 3458A multimeter as voltage source and current meter, respectively.

3. Results and discussion

3.1. Structure and composition of gas sensing nanoparticles

According to X-ray photoelectron spectroscopy (XPS) (Fig. 1), the nanoparticles encompassed mixed oxidation states of the corresponding metals, except in the case of silver which was found to be entirely metallic (Ag $3d_{5/2}$ at 368.4 eV). The resolved Pd $3d_{5/2}$ peaks at 336.3, 337.5 and 338.5 eV binding energies suggest the oxidation states of Pd^{2+} and Pd^{4+} present in the samples (PdO, PdO_2, $Pd(acac)_2$). In the case of platinum modified powders, both metallic Pt^0 and oxidized states such as Pt^{2+} and Pt^{4+} coexist according to the fitted Pt $4f_{7/2}$ peak positions at 71.2, 72.9 and 75.1 eV, respectively.

The decomposition of metal-precursors impregnated on the WO_3 nanoparticles resulted in the formation of particles with a few nanometers in size on the surface (Fig. 2). The typical size of the particles formed was between 1–4 nm, 2–5 nm and 1–2 nm from the $AgNO_3$, $Pd(C_5H_7O_2)_2$, and $Pt(C_5H_7O_2)_2$ precursors, respectively. The decomposition products of the impregnated $AgNO_3$ appear separately on the WO_3 surface, while the $Pd(C_5H_7O_2)_2$ precursor produces nanoparticles that are agglomerated to larger clusters of ~10 nm size. In the case of $Pt(C_5H_7O_2)_2$ precursor, the formed nanoparticles show only minor agglomeration.

The distribution of nanoparticles was not completely uniform as revealed by lower magnification transmission electron microscopy (TEM) analysis. The values of average metal concentration in the powder samples ($c_{Ag} = 1.0 \pm 0.6$ wt%, $c_{Pd} = 0.9 \pm 0.5$ wt%, $c_{Pt} = 1.4 \pm 0.5$ wt%), measured by energy-dispersive X-ray spectroscopy (EDX), are close to the designed value ($c_{Me} = 1$ wt%). However, the considerable standard deviation in each dataset also hints at non-uniform distribution of anchored nanoparticles on the WO_3 surface.

Because of their small size, the low concentration and probably also due to the amorphous structure of the deposited nanoparticles, neither the reduced nor any oxide phases of the

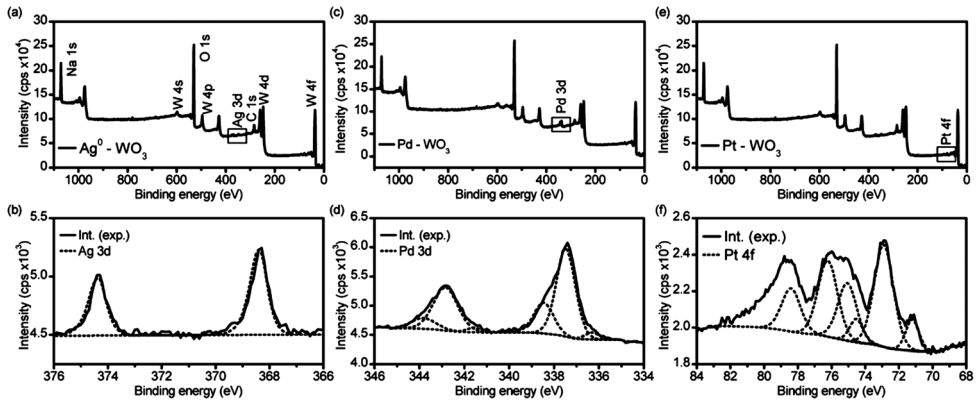

Fig. 1 X-ray photoelectron spectra of the decorated WO_3 nanoparticles. In the case of Pt–WO_3, not-fitted intensity at 79 eV corresponds to W 5s core level.

metals could be identified by means of XRD analysis. Each pattern is very similar to that of the original monoclinic WO_3 (JCPDS card #830951) as shown in Fig. 3. The crystallite size of the WO_3 support was evaluated to be 32 ± 3 nm based on the broadening of the (004) and (040) peaks. Broad reflections at $2\Theta < 15^\circ$ of Ag–WO_3 and Pd–WO_3 data originate from saturation of the XRD facility sensor at low angles with high intensity radiation and thus are not from the sample powders.

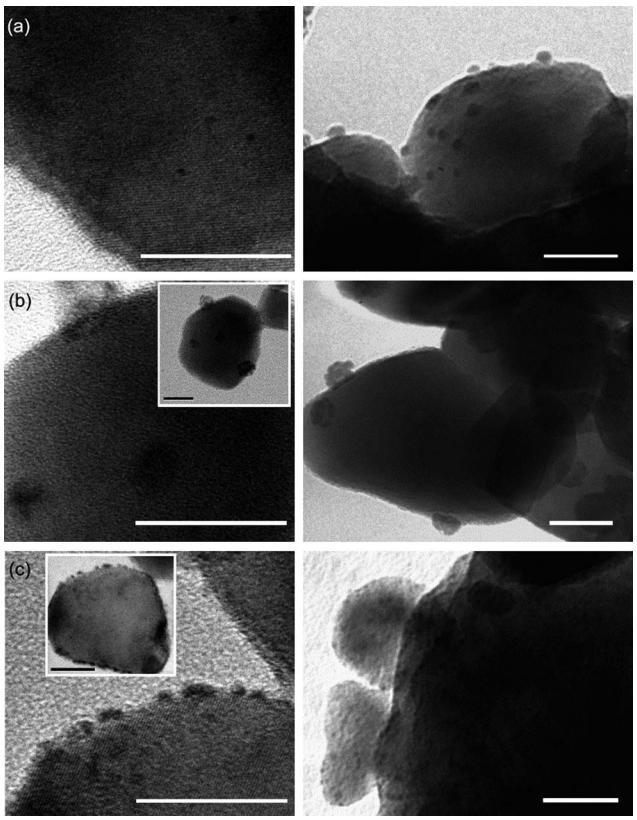

Fig. 2 High-resolution (left column) and energy filtered (right column) transmission electron microscopy images of decorated WO_3 nanoparticles applied in the gas sensing measurements. The nanoparticles deposited on the WO_3 surfaces are the decomposition products of (a) $AgNO_3$, (b) $Pd(C_5H_7O_2)_2$ and (c) $Pt(C_5H_7O_2)_2$ precursors. Insets show decorated individual WO_3 nanocrystals. Scale bars show 20 nm.

3.2. Stability of nanoparticle suspensions and average size of nanoparticles

In order to determine the stability of the aqueous suspensions of nanoparticles further used for inkjet printing and estimate average particle diameters, we performed spectroscopic measurements. Collimated transmittance of a narrow beam (0.5 mm in diameter) scanned over the 250–1100 nm wavelengths through the original suspensions was measured; calibration was done using water. The spectra did not change within at least 3 h for all WO_3 nanoparticle suspensions (both decorated and pristine).

Average nanoparticle sizes were estimated by the comparison of scattering coefficients (μ_s) retrieved from the measured data and derived from the Mie theory of light scattering for a light wavelength of 650 nm. At such a wavelength, no absorption takes place, thus collimated transmittance (T_c) obeys the Beer's law: $T_c = e^{-\mu s L}$, where L is the physical thickness of the cuvette with the suspension (10 mm). On the other hand, the scattering coefficient for different particle diameters was calculated from the Mie theory, using refractive index of water (1.33) and WO_3 (2.3), concentrations of the inks, and WO_3 density (7.16 g cm^{-3}). Since the concentration values are not exact but have some uncertainty, the theoretical values have also upper and lower limits (Fig. 4, for Pt–WO_3 as an example).

The values of the scattering coefficient obtained from the experiment should match those derived from the theory, thus

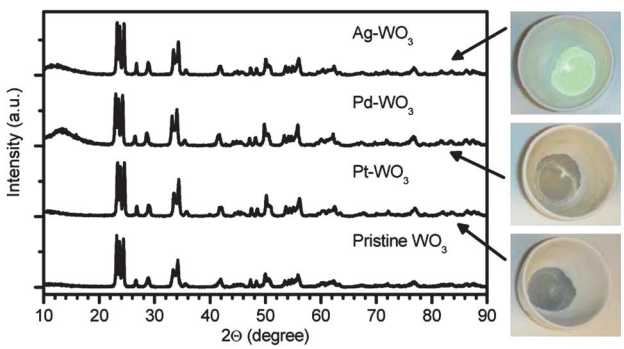

Fig. 3 X-ray diffraction patterns of pristine and the three different types of decorated WO_3 nanoparticles.

giving us the particle diameters: 119 ± 3 nm (pristine WO_3), 118 ± 6 nm (Pt–WO_3), 109 ± 2 nm (Pd–WO_3), and 103 ± 16 nm (Ag–WO_3). The value measured for pristine WO_3 by means of dynamic light scattering analysis (Delsa Nano C) was also found to be very similar: 100 ± 40 nm. Zeta potential measurements (Delsa Nano C) indicate that the dispersion has good stability. When the pristine WO_3–water ink was diluted with distilled water (10 mM NaCl solution) (1 : 10), the zeta potential was measured to be −44 mV ± 5 mV (53 mV ± 5 mV), respectively. Based on these observations, the prepared suspensions are concluded to be stable, having dispersed particles of 110 ± 20 nm in diameter.

3.3. Inkjet deposited sensor chips

To obtain dispersions for inkjet deposition, the as-prepared nanoparticle powders were suspended in deionized water using ultrasonic agitation. To reveal the printability of our inks, 3 different types of patterns were deposited first on a Si wafer.

The first pattern consisted of only individual dots as shown in Fig. 5(a). The other pattern, as in Fig. 5(b), was made by depositing 4 droplets rapidly next to each other with 25 μm centre-to-centre spacing and ~0.2 ms delay. The third type of pattern is similar to the previous one but the subsequent droplets are ejected with ~1.8 s delay (Fig. 5(c)). In all cases, single (1 layer) and multilayer (3, 9 and 27 layers) deposits were made as well. Droplets deposited in a single location reveal that at least 9 repeated layers are needed to achieve continuous nanoparticle films. When the droplets are printed next to each other they tend to merge together forming an elongated but not line shaped pattern. Accordingly, to be able to fabricate well defined sensor patterns, it is essential to allow the droplets to dry before the placing of the subsequent one.

After printing on the sensor chips, the dried WO_3 patterns were observed to form a porous, thick and continuous layer with well-defined edges (Fig. 6). The typical resistance of the printed sensor structures (depending on doping and fabrication batch) was between 10 MΩ and 1 GΩ at 220 °C. The current–voltage characteristics of the sensors show slight non-linear behaviour (not shown), which is understandable considering the Schottky interface between the large work function chip-electrode

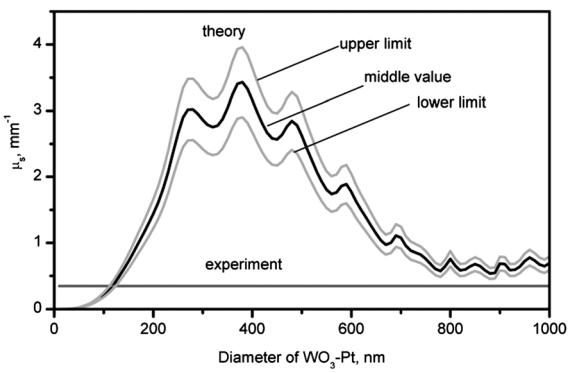

Fig. 4 Scattering coefficients for Pt–WO_3 nanoparticle suspension *vs.* particle diameter: curves are derived from theory and straight line is from experiment. The intersection gives the average particle size.

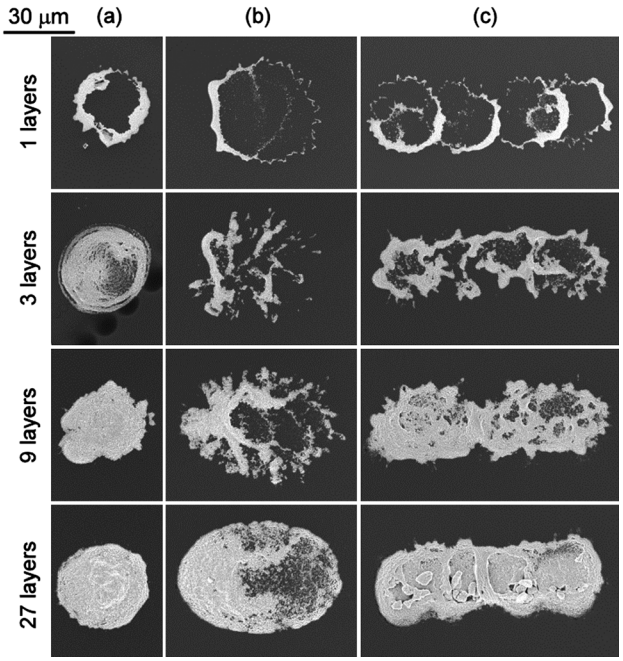

Fig. 5 WO_3 nanoparticle inkjet test patterns. (a) A droplet deposited in a single location 1, 3, 9 and 27 layers. Four droplets printed in a row with 25 μm spacing using (b) ~0.2 ms and (c) ~1.8 s drying time between depositions of subsequent adjacent droplets. Notice: at least 5 seconds drying time was allowed in each case between printing of subsequent layers.

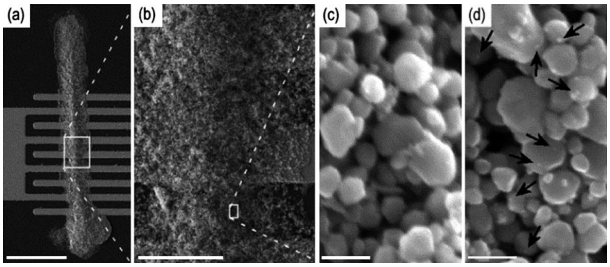

Fig. 6 Field emission scanning electron micrographs of a sensor with printed WO_3 nanoparticles (a–c). Panel (d) shows a higher magnification image of palladium oxide decorated WO_3 nanoparticles on a sensor. The black arrows indicate the decorating palladium oxide particles of 2–5 nm size. Scale bars show 50 μm, 10 μm, 100 nm and 100 nm in the (a), (b), (c) and (d) panels, respectively.

($\varphi_{Pt} \sim 5.7$ eV and $\varphi_{Ti} \sim 4.3$ eV)[37] and the n-type semiconducting WO_3 surface ($\chi_{WO_3} \sim 3.3$ eV).[38]

3.4. Gas adsorption behaviour on metal and metal-oxide surfaces

Quite many of the n-type semiconducting metal oxides, such as WO_3, SnO_2 and ZnO, display strong activity towards sensing of environmentally and industrially relevant gases including CO, CH_4, H_2 NH_3, NO_x, *etc.*[39,40] According to a simple qualitative picture, reducing gases adsorbed on the oxide surfaces (n-type) increase electrical conductivity by inducing oxygen defects, which are essential for ionic conduction in the lattice. Oxidizing

analytes – on the other hand – work opposite and decrease conductivity. The degree of change is a function of the chemistry and concentration of analytes, and of course depends on the sensor material itself. However, the presence of the decorating metal/metal oxide nanoparticles on the surface of semiconducting metal oxides is clearly making the overall picture of gas sorption and sensing mechanisms more complex.

The sensitivity of our printed WO_3 based devices towards a particular analyte varies greatly with the decorating metal or metal oxide in question, thus inducing molecular selectivity, *i.e.* discrimination of different types of analytes. The response and recovery times (95% and 5% of the saturation conductance in reference to the base line, respectively) depend also on the type of the prepared device. The quickest sensor is the Pt–WO_3, with a typical response time of a few minutes. All other sensors display slower responses of ~10 minutes or higher, except the pristine WO_3, which responded to H_2S or NO within 3 minutes. Sensor recovery usually requires longer time-periods, typically half an hour or more (Fig. 7) being higher than those typical for Taguchi-type gas sensors.[41,42] Both the large specific surface area of the WO_3 nanoparticle based sensing materials and the porous nature of the deposited patterns on the chips can be responsible for this. While the large surface area is influencing the rates of adsorption and desorption; the porous structure is limiting diffusion of the gas molecules from/to the nanoparticles.

Noticeable drift is present – mainly – at the beginning of individual gas measurements. This is a common phenomenon seen in most metal oxide gas sensors caused by several factors: the slow desorption of gas molecules from the surface, bulk diffusion of oxygen vacancies in the oxide, change of semiconductor–metal contact at the electrodes, and physical changes in the sensors' structure such as crack formation and coarsening of sensitizing particles, *etc.*[43,44] Anyhow, fairly stable base signals could be achieved after a few hours of heat treatment at 220 °C.

3.4.1. Nitrogen monoxide – NO. Each sensor was found to be sensitive towards NO with varying response depending on the type of the decoration metal. Upon exposure to oxidizing gases, the electrical conductance decreased, as expected for a sensor based on the n-type semiconducting active layer. In previous studies, WO_3 sensors were observed to exhibit an enhanced response to NO, when doped with Ag[45] or covered by a thin layer of Pt or Pd.[11] In another study, the WO_3 gas sensor with NiO-doping was shown to have enhanced NO response, when NiO concentration was in the range of 1 wt%.[46] However, in our case the response to NO was observed to be slightly lower for metal and metal oxide decorated WO_3. An interesting feature was observed when measuring NO analyte with Pd decorated sensors. At low NO concentrations (0.5 and 2 ppm), an increase in the conductance was observed indicating that the surface of the

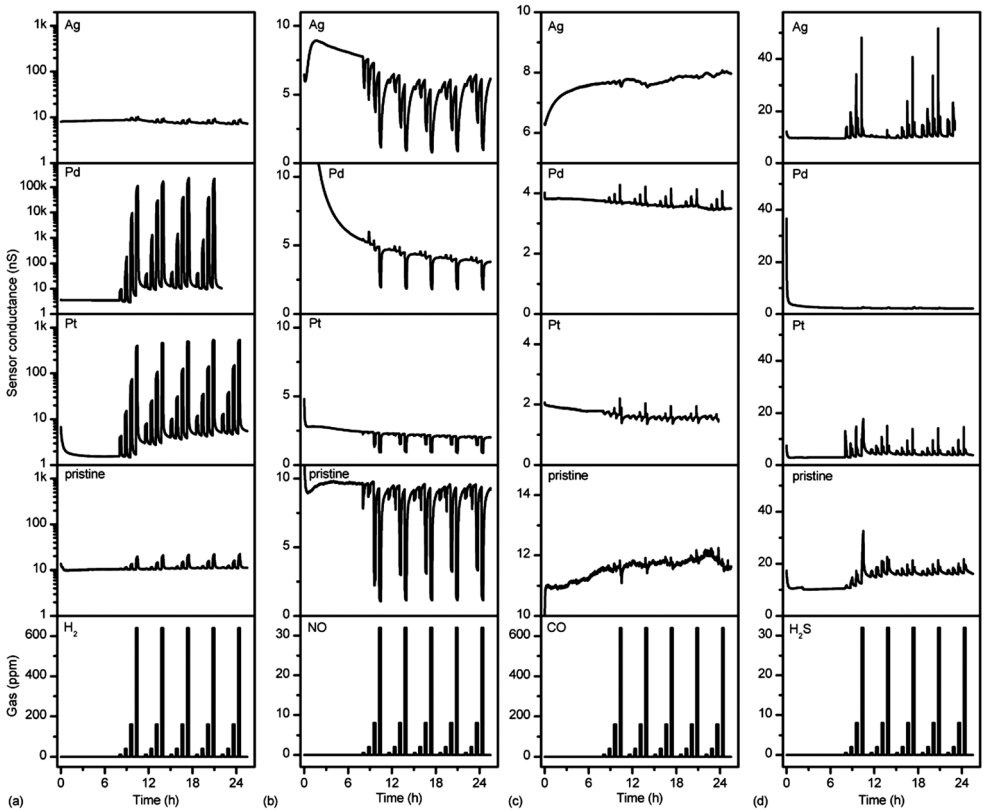

Fig. 7 Change in the conductance of the modified and pristine WO_3 nanoparticle based gas sensors when exposed in the following order to (a) 10, 40, 160, and 640 ppm of H_2, (b) 0.5, 2, 8, and 32 ppm of NO, (c) 10, 40, 160, and 640 ppm of CO, and (d) 0.5, 2, 8, and 32 ppm of H_2S analytes in synthetic air carrier gas at 220 °C. In each experiment, 5 subsequent sets of pulses were applied to demonstrate sensor recovery and repeatability of gas responses. Please note that the *y*-axes in the H_2 sensing data are logarithmic.

sensor nanoparticles was either slightly reduced or at least some of the adsorbed oxygen species (of the carrier gas) desorbed. Based on extended X-ray absorption fine structure (EXAFS)[47] analysis and IR[48] measurements, the reduction of Pd^{2+} to Pd^{1+} with adsorbed NO is, indeed, possible resulting in the formation of NO_2 gas. At higher NO concentrations, the amount of produced and adsorbed NO_2, obviously an oxidizing gas, may overcome the reductive behaviour of NO, thus expressing a more pronounced oxidative gas response of the sensors.[49]

It is worth mentioning that WO_3 itself is not reported as an effective catalyst for the oxidation of NO. Anyhow, our results suggest that NO undergoes oxidation on our sensors, which may be due to the presence of Pt in each sample (the electrode surfaces), in addition to the other metals/metal oxides decorating the WO_3 nanoparticles.[45,50–56]

3.4.2. Hydrogen sulphide – H_2S. Dwyer *et al.*[57] have used XPS to investigate the interactions between tungsten oxide films and H_2S gas at 475 K, close to our sensor operation temperature of 493 K. The WO_3 film was exposed to different concentrations of H_2S gas and after each exposure, W 4f, O 1s and S 2p spectra were recorded. It was assumed that in the first step, oxygen vacancies are formed on the surface of the crystal. Also other mechanisms such as the development of a WS_2 surface may evolve similarly to those on multitude transition-metal oxides when exposed to H_2S.[58,59] Presumably, at low concentrations, H_2S dissociatively adsorbs on the surface and desorbs as SO_2 and H_2O, consequently resulting in oxygen vacancies in the lattice. Large quantities of hydrogen-sulphide promote the evolution of tungsten-sulphide on the surface of WO_3. This partial poisoning of the surface may explain why the first set of gas pulses induced larger responses than the subsequent ones.

Pt-decorated sensors show only small reductive gas response, while the Pd-decorated devices demonstrate practically no response at all. In these cases, a strong metal surface poisoning with the formation of palladium- and platinum sulphides[60] can reasonably explain such a poor sensing behaviour.

In the case of Ag-decorated WO_3, a surface layer of Ag_2S forms when the nanoparticles are exposed to H_2S, especially in the presence of O_2 at the same time.[61] Though the sulphide layer is thermally unstable at elevated temperatures after measurements in H_2S,[62,63] the metal decorated nanoparticles can only partially recover at 220 °C under air flow leading to a decreased sensor performance (Fig. S1†).

3.4.3. Hydrogen – H_2. The relatively moderate responses of pristine WO_3 and Ag-decorated sensors result from the absence or limited catalytic oxidation of H_2 below 400 °C.[64] However, due to the Pt electrodes, some electrons and protons form after the dissociation of H_2 to adsorbed H atoms, and the protons can react with lattice oxygen of WO_3, thus creating oxygen vacancies and an increased conductance.[65–67]

Both platinum and palladium decorated WO_3 gas sensors were observed to be highly sensitive (~10% per ppm and ~1000% per ppm, respectively) and selective towards H_2. The Pt-decorated sensor illustrated an extremely high $\sim 10^4$-fold increase in its conductance when exposed to 640 ppm analyte (Fig. 7). The oxides of noble metals, such as Pd and Pt, are reduced in H_2 at 220 °C. Consequently, it is highly likely that on Pd/WO_3 as well as on Pt/WO_3 surfaces, H_2 is dissociatively adsorbed, which in turn may cause the reduction of W^{6+} centers, consequently increasing the number of strong acid sites of WO_3,[68] as also demonstrated[69] Pt or Pd impregnated WO_3 catalyzes H_2 oxidation. Our results on Pt and Pd modified WO_3 are comparable with earlier reports on Pt decorated ZnO nanorods[70] and nanoparticles[14] as highly sensitive H_2 sensors. The main reason for the extremely high sensitivity towards H_2 is most likely due to a spillover of dissociated hydrogen that facilitates reduction of the WO_3 surface in a similar manner to the directly adsorbed H_2.

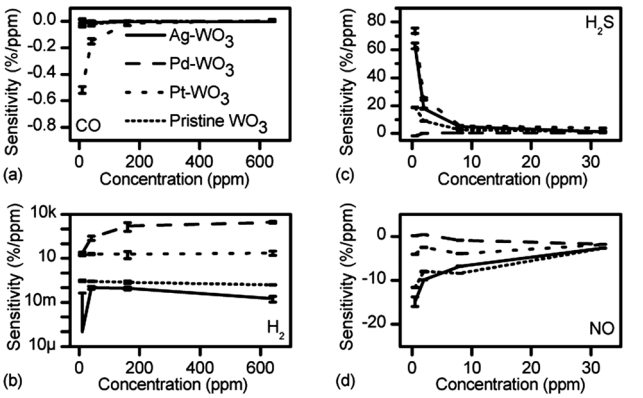

Fig. 8 Gas sensitivities (as a function of analyte concentration) of metal decorated and pristine WO_3 sensors to (a) CO, (b) H_2, (c) H_2S, and (d) NO.

3.4.4. Carbon monoxide – CO. In the case of CO catalysis, adsorption of CO molecules onto the metal oxide surface usually takes place *via* the C atom on the metal cations. As the next step, an O atom of the oxide surface can be transferred to the adsorbed radical/CO molecule, leading to the formation of (i) oxygen vacancies in the metal oxide and (ii) release of CO_2 from the surface. The catalyst can be regenerated by the chemisorption of O_2 molecules from the gas phase, thus facilitating the re-oxidation of the surface for subsequent CO oxidation and so forth.[40] This sequence of events (*i.e.* Mars–van Krevelen mechanism) will result in a dynamic change of lattice oxygen/defect concentration ultimately leading to a change (increase) in the materials conductivity.[71] On the contrary, in our system the sensor surface is always flooded with oxygen species because of the sensor recovery in air atmosphere in between the gas pulses. One should also observe the high concentration of O_2 in the buffer gas. Accordingly, the decorating nanoparticles should be covered by adsorbed and dissociated oxygen species. Since the surface is practically blocked for CO to adsorb, the Eley–Rideal mechanism seems to be the only plausible way to oxidize the analyte to CO_2 (ref. 72 and 73) and therefore does not give rise to any kind of change of the electrical properties as a result of this phenomenon. Since CO has a limited access to the surface, the sensitivity of the devices for CO is generally poor (Fig. 7).

4. Conclusions

Tungsten oxide nanoparticles decorated by wet impregnation with metal and metal oxide nanoparticles and subsequently subject to inkjet printing were applied to construct Taguchi-type

metal oxide gas sensors based on modified WO_3 nanoparticles. Gas responses of the sensors were observed to vary depending on the surface decoration. The relative change of conductance for Pd and Pt modified sensors, when exposed to 640 ppm of H_2 were extremely high, ~100-fold and ~10 thousand-fold, respectively. The responses of Ag-modified and pristine WO_3 sensors towards NO were considerable (~10% per ppm analyte for both), while the Pd and Pt modified nanoparticles demonstrated a moderate response. In general, the responses of the devices towards CO and H_2S were observed to be low (Fig. 8). The large differences in the sensitivities therefore demonstrate that metal or metal oxide decorated WO_3 nanoparticles are suitable for selective detection of analytes.

Besides the simplicity of inkjet printing to produce different types of sensor devices with high throughput, it is also a cost effective approach with practical relevance. When printing several sensors in a single batch, the sensing layer for a single device may be deposited within a fraction of a second. The amount of WO_3 nanomaterials used in a single component is estimated to be around nanogram quantities resulting in less than one Euro material cost per 1 million devices. Even though this work introduced printing of WO_3 nanoparticles between Pt electrodes on Si/SiO_2 substrates, an analogous inkjet printing method could be applied on virtually any kind of substrate. Accordingly, the manufacturing cost of such sensors is evaluated to depend almost completely on the price of the measuring electronics.

Though we have attempted to explain the observed sensor responses on the basis of catalytic surface processes reported in the literature on similar gas–solid systems, a more precise and exact evaluation of the surface reactions requires further investigation using for instance *in situ* infrared and X-ray photoelectron spectroscopy methods.

Acknowledgements

The authors thank Niina Halonen and Jani Mäklin for technical assistance. Financial support from TEKES (Segase, Intag and AutoSys projects) and Academy of Finland (RoCaNaMe project) is acknowledged. J.K. acknowledges the position at Graduate School of Infotech Oulu (Finland), and the grants received from the Riitta and Jorma J. Takanen, Emil Aaltonen and Tauno Tönning Foundations. G.T. acknowledges the academy researcher post of the Academy of Finland. K.K. and J.-P.M. are grateful for support from Bio4Energy programme, Knut and Alice Wallenberg and Kempe Foundations.

References

1 K. Shaner and H. L. Tuller, *J. Electroceram.*, 2004, **24**, 177–199.
2 J. Kukkola, E. Jansson, A. Popov, J. Lappalainen, K. Kordas, N. Halonen, J. Hast, K. Jokinen, T. Fabritius, H. Jantunen, R. Myllylä, A. Vasiliev and N. Zaretskiy, unpublished work.
3 M. Akiyama, J. Tamaki, N. Miura and N. Yamazoe, *Chem. Lett.*, 1991, 1611–1614.
4 C. Cantalini, H. T. Sun, M. Faccio, M. Pelino, S. Santucci, L. Lozzi and M. Passacantando, *Sens. Actuators, B*, 1996, **31**, 81–87.
5 C. Balazsi, K. Sedlackova, E. Llobet and R. Ionescu, *Sens. Actuators, B*, 2008, **133**, 151–155.
6 Y. Zhao, Z. Feng and Y. Liang, *Sens. Actuators, B*, 2000, **66**, 171–173.
7 J. L. Solis, S. Saukko, L. Kish, C. G. Granqvist and V. Lantto, *Thin Solid Films*, 2001, **391**, 255–260.
8 M. Penza and L. Vasanelli, *Sens. Actuators, B*, 1997, **41**, 31–36.
9 T. Siciliano, A. Tepore, G. Micocci, A. Serra, D. Manno and E. Filippo, *Sens. Actuators, B*, 2008, **133**, 321–326.
10 H. Xia, Y. Wang, F. Kong, S. Wang, B. Zhu, X. Guo, J. Zhang, Y. Wang and S. Wu, *Sens. Actuators, B*, 2008, **134**, 133–139.
11 M. Penza, C. Martucci and G. Cassano, *Sens. Actuators, B*, 1998, **50**, 52–59.
12 J. Zhang, X. Liu, S. Wu, M. Xu, X. Guo and S. Wang, *J. Mater. Chem.*, 2010, **20**, 6453–6459.
13 W. Zheng, X. Lu, W. Wang, Z. Li, H. Zhang, Z. Wang, X. Xu, S. Li and C. Wang, *J. Colloid Interface Sci.*, 2009, **338**, 366–370.
14 C. S. Rout, A. R. Raju, A. Govindaraj and C. N. R. Rao, *Solid State Commun.*, 2006, **138**, 136–138.
15 R. K. Joshi, Q. Hu, F. Alvi, N. Joshi and A. Kumar, *J. Phys. Chem. C*, 2009, **113**, 16199–16202.
16 E. Burstein, *Phys. Rev.*, 1954, **93**, 632–633.
17 T. S. Moss, *Proc. Phys. Soc., London, Sect. B*, 1954, **67**, 775–782.
18 G. A. Niklasson and C. G. Granqvist, *J. Mater. Chem.*, 2007, **17**, 127–156.
19 N. Yamazoe, G. Sakai and K. Shimanoe, *Catal. Surv. Asia*, 2003, **7**, 63–75.
20 A. De Girolamo Del Mauro, I. A. Grimaldi, F. Loffredo, E. Massera, T. Polichetti, F. Villani and G. Di Francia, *J. Appl. Polym. Sci.*, 2011, **122**, 3644–3650.
21 H. Lee, G. Shaker, K. Naishadham, S. Xiaojuan, M. McKinley, B. Wagner and M. Tentzeris, *IEEE Trans. Microwave Theory Tech.*, 2011, **59**, 2665–2673.
22 K. Crowley, A. Morrin, R. L. Shepherd, M. in het Panhuis, G. G. Wallace, M. R. Smyth and A. J. Killard, *IEEE Sens. J.*, 2010, **10**, 1419–1426.
23 V. Dua, S. Surwade, S. Ammu, S. Agnihotra, S. Jain, K. Roberts, S. Park, R. Ruoff and S. Manohar, *Angew. Chem., Int. Ed.*, 2010, **49**, 2154–2157.
24 M. F. Mabrook, C. Pearson, A. S. Jombert, D. A. Zeze and M. C. Petty, *Carbon*, 2009, **47**, 752–757.
25 J. Kim, J. Yun, J. Song and C. Han, *Sens. Actuators, B*, 2009, **135**, 587–591.
26 L. Yang, R. Zhang, D. Staiculescu, C. P. Wong and M. M. Tentzeris, *IEEE Antennas Wireless Propagat. Lett.*, 2009, **8**, 653–656.
27 K. Crowley, A. Morrin, A. Hernandez, E. O'Malley, P. G. Whitten, G. G. Wallace, M. R. Smyth and A. J. Killard, *Talanta*, 2008, **77**, 710–717.
28 H. Haspel, R. Ionescu, P. Heszler, Á. Kukovecz, Z. Kónya, Z. Gingl, J. Mäklin, T. Mustonen, K. Kordás, R. Vajtai and P. M. Ajayan, *Phys. Status Solidi B*, 2008, **245**, 2339–2342.
29 J. Mäklin, T. Mustonen, N. Halonen, G. Tóth, K. Kordás, J. Vähäkangas, H. Moilanen, Á. Kukovecz, Z. Kónya, H. Haspel, Z. Gingl, P. Heszler, R. Vajtai and P. M. Ajayan, *Phys. Status Solidi B*, 2008, **245**, 2335–2338.
30 N. Cho, T. Lim, Y. Jeon and M. Gong, *Macromol. Res.*, 2008, **16**, 149–154.
31 W. R. Small and M. Panhuis, *Small*, 2007, **3**, 1500–1503.
32 K. Kordás, T. Mustonen, G. Tóth, H. Jantunen, M. Lajunen, C. Soldano, S. Talapatra, S. Kar, R. Vajtai and P. M. Ajayan, *Small*, 2006, **2**, 1021–1025.
33 B. Li, S. Santhanam, L. Schultz, M. Jeffries-EL, M. C. Iovu, G. Sauvé, J. Cooper, R. Zhang, J. C. Revelli, A. G. Kusne, J. L. Snyder, T. Kowalewski, L. E. Weiss, R. D. McCullough, G. K. Fedder and D. N. Lambeth, *Sens. Actuators, B*, 2007, **123**, 651–660.
34 M. F. Mabrook, C. Pearson and M. C. Petty, *IEEE Sens. J.*, 2006, **6**, 1435–1444.
35 M. F. Mabrook, C. Pearson and M. C. Petty, *Sens. Actuators, B*, 2006, **115**, 547–551.
36 A. Bietsch, J. Zhang, M. Hegner, H. P. Lang and C. Gerber, *Nanotechnology*, 2004, **15**, 873.
37 T. Mori, T. Kozawa, T. Ohwaki, Y. Taga, S. Nagai, S. Yamasaki, S. Asami, N. Shibata and M. Koike, *Appl. Phys. Lett.*, 1996, **69**, 3537–3539.
38 F. Liu, L. Li, F. Mo, J. Chen, S. Deng and N. A. Xu, *Cryst. Growth Des.*, 2010, **10**, 5193–5199.
39 A. A. Tomchenko, G. P. Harmer, B. T. Marquis and J. W. Allen, *Sens. Actuators, B*, 2003, **93**, 126–134.
40 J. Hagen, *Industrial Catalysis: A Practical Approach*, Wiley-VCH, Weinheim, 2006.

41 G. Korotcenkov, S. D. Han and J. R. Stetter, *Chem. Rev.*, 2009, **109**, 1402–1433.
42 A. Afzal, N. Cioffi, L. Sabbatini and L. Torsi, *Sens. Actuators, B*, 2012, DOI: 10.1016/j.snb.2012.05.026 (online first).
43 S. Di Carlo and M. Falasconi, Drift Correction Methods for Gas Chemical Sensors in Artificial Olfaction Systems: Techniques and Challenges, in *Advances in Chemical Sensors*, ed. Wen Wang, InTech, 2012, pp. 305–326.
44 G. Korotcenkov, *Sens. Actuators, B*, 2005, **107**, 209–232.
45 L. Chen and S. C. Tsang, *Sens. Actuators, B*, 2003, **89**, 68–75.
46 J. Park, K. Hong, W. Lee and Y. Shin, *Jpn. J. Appl. Phys., Part 2*, 2001, **40**, L967–L969.
47 K. Okumura, J. Amano, N. Yasunobu and M. Niwa, *J. Phys. Chem. B*, 2000, **104**, 1050–1057.
48 C. Descorme, P. Gélin, M. Primet and C. Lécuyer, *Catal. Lett.*, 1996, **41**, 133–138.
49 H. H. Kung, *Transition Metal Oxides: Surface Chemistry and Catalysis*, Elsevier, New York, 1991.
50 H. T. Karlsson and H. S. Rosenberg, *Ind. Eng. Chem. Process Des. Dev.*, 1984, **23**, 808–814.
51 R. B. Getman and W. F. Schneider, *J. Phys. Chem. C*, 2007, **111**, 389–397.
52 E. Xue, K. Seshan and J. R. H. Ross, *Appl. Catal., B*, 1996, **11**, 65–79.
53 J. Dawody, M. Skoglundh and E. Fridell, *J. Mol. Catal. A: Chem.*, 2004, **209**, 215–225.
54 H. Tsukahara, T. Ishida and M. Mayumi, *Nitric Oxide*, 1999, **3**, 191–198.
55 J. Kukkola, J. Mäklin, N. Halonen, T. Kyllönen, G. Tóth, M. Szabó, A. Shchukarev, J. Mikkola, H. Jantunen and K. Kordás, *Sens. Actuators, B*, 2011, **153**, 293–300.
56 M. Levy and T. Pagnier, *Sens. Actuators, B*, 2007, **126**, 204–208.
57 B. Frühberger, M. Grunze and D. J. Dwyer, *Sens. Actuators, B*, 1996, **31**, 167–174.
58 A. Steinbrunn and C. Lattaud, *Surf. Sci.*, 1985, **155**, 279–295.
59 Y. Okamoto, H. Tomioka, Y. Katoh, T. Imanaka and S. Teranishi, *J. Phys. Chem.*, 1980, **84**, 1833–1840.
60 P. Albers, J. Pietsch and S. F. Parker, *J. Mol. Catal. A: Chem.*, 2001, **173**, 275–286.
61 J. L. Elechiguerra, L. Larios-Lopez, C. Liu, D. Garcia-Gutierrez, A. Camacho-Bragado and M. J. Yacaman, *Chem. Mater.*, 2005, **17**, 6042–6052.
62 D. L. Douglass, *Sol. Energy Mater.*, 1984, **10**, 1–7.
63 D. Zivkovic, M. Sokic, Z. Zivkovic, D. Manasijevic, Lj. Balanovic, N. Strbac, V. Cosovic and B. Boyanov, *J. Therm. Anal. Calorim.*, 2012, DOI: 10.1007/s10973-012-2300-z (online first).
64 L. Sha and Z. J. Qiu, *Int. J. Refract. Met. Hard Mater.*, 2008, **26**, 362–366.
65 H. Nakagawa, N. Yamamoto, S. Okazaki, T. Chinzei and S. Asakura, *Sens. Actuators, B*, 2003, **93**, 468–474.
66 M. Matsumiya, W. Shin, N. Izu and N. Murayama, *Sens. Actuators, B*, 2003, **93**, 309–315.
67 J. Z. Ou, M. H. Yaacob, M. Breedon, H. D. Zheng, J. L. Campbell, K. Latham, J. du Plessis, W. Wlodarski and K. Kalantar-zadeh, *Phys. Chem. Chem. Phys.*, 2011, **13**, 7330–7339.
68 D. G. Barton, S. L. Soled and E. Iglesia, *Top. Catal.*, 1998, **6**, 87–99.
69 V. K. Yatsimirskii, V. V. Lesnyak, I. N. Gut and O. Y. Boldyreva, *Theor. Exp. Chem.*, 2005, **41**, 329–333.
70 H. T. Wang, B. S. Kang, F. Ren, L. C. Tien, P. W. Sadik, D. W. Norton, S. J. Pearton and J. Lin, *Appl. Phys. Lett.*, 2005, **86**, 243503.
71 V. E. Henrich and P. A. Cox, *The Surface Science of Metal Oxides*, Cambridge University Press, Cambridge, 1994.
72 J. T. Hirvi, T. J. Kinnunen, M. Suvanto, T. A. Pakkanen and J. K. Norskov, *J. Chem. Phys.*, 2010, **133**, 084704.
73 G. W. Keulks and C. C. Chang, *J. Phys. Chem.*, 1970, **74**, 2590–2595.

